High-speed X-Ray Phase-Contrast Imaging of String Cavitation in an Enlarged Diesel-Injector Orifice Replica

I.K. Karathanassis[*1], P. Koukouvinis[1], M. Lorenzi[1], E. Kontolatis[1], Z. Li[2], J. Wang[2],
N. Mitroglou[1] and M. Gavaises[1]
[1]School of Mathematics, Computer Science and Engineering, City, University of London, UK
[2]Advanced Photon Source, Argonne National Laboratory, Lemont, IL 60439, USA
*Corresponding author: Ioannis.Karathanassis@city.ac.uk

Abstract

The present investigation illustrates the temporally-resolved, phase-contrast visualization of the cavitating flow within an enlarged injector replica conducted at the ANL Advanced Photon Source. The flow was captured through side-view, x-ray radiographies at 67890 frames per second with an exposure time of 347ns. The orifice employed for the experiments has an internal diameter of 1.5mm and length equal to 5mm. A parametric investigation was conducted considering various combinations of the Reynolds and cavitation numbers, which designate the extent of in-nozzle cavitation. Proper post-processing of the obtained radiographies enabled the extraction of information regarding the shape and dynamical behaviour of cavitating strings. The average string extent along with its standard deviation was calculated for the entire range of conditions examined (Re=18000-36000, CN=1.6-7.7). Furthermore, the effect of the prevailing flow conditions on quantities indicative of the string dynamic behaviour such as the break-up frequency and lifetime was characterized and the local velocity field in the string region was obtained.

Keywords

Fuel injection, synchrotron radiation, nozzle flow, high-speed radiography, velocimetry

Introduction

Modern fuel injectors operate at extreme pressures of the order of 3000 bars, as it has been demonstrated that this degree of pressurization leads to increased engine performance and reduced pollutant emissions [1]. The turbulent nature of injector flows gives rise to highly-transient cavitation phenomena emanating due to the geometrical layout and/or the emerging secondary flow pattern [2]. The onset of vortical (string) cavitation within the injector holes has been demonstrated to lead to atomization enhancement and spray cone angle increase [3]. In contrast, as demonstrated in [4], the collapse of unstable vapour clouds appears to be more aggressive compared to attached cavities in terms of cavitation-induced erosion.

Referring to two-phase flow visualization, optical techniques, e.g. shadowgraphy, Schlieren or LIF/LIEF imaging, have been traditionally employed and thus a transparent, durable material such as Perspex or sapphire must be utilized for the manufacturing of the nozzles. Several experimental investigations dealing with the characterization of the cavitating flow arising within fuel injectors have been performed on enlarged nozzle replicas [5], since the lower pressure of injection along with the larger geometrical length scale compared to real-size injectors facilitate the attainment of higher temporal and spatial resolution and, thus, allow a more thorough elucidation of the flow phenomena setting in. Concurrent studies having been conducted on real-size injectors with transparent tips have verified the main conclusions established by the investigations on replicas with regard to the flow topology and main features [6]. Flow similarity between the different examinations performed on varying length scales is ensured by the adjustment of the non-dimensional quantities that designate the flow conditions, i.e. the cavitation (CN) and Reynolds (Re) numbers.

X-ray imaging is currently gaining momentum as a technique suitable for the visualization of two-phase flows with relevance to fuel injectors. Both x-ray phase-contrast and attenuation imaging have been performed so as to illustrate the spray structure and local flow dynamics in the near-nozzle region [7-8]. The work of [7] visualized the spray expelled by a single and a three-hole injector configuration using X-ray Phase Contrast Imaging (XPCI) and provided quantitative data on the axial velocity and turbulence intensity up to a location of approximately 50mm downstream the nozzle outlet. Besides, in [8], by making use of x-ray attenuation imaging, provided quantitative data for the spray density in a region up to 10mm downstream the outlet of a single-orifice injector. Referring to in-nozzle flows, [9] quantified the vapour extent that emerged within an enlarged orifice, while they also managed to obtain time-resolved measurements, yet for a very small area of interest of the order of μm^2. More recently, the group of the authors [10] relied on micro-computed tomography to obtain the average three-dimensional structure and vapour volume fraction distribution of the cloud cavitation that arose in a simplified injector layout with an orifice

diameter of 3mm. In this study, an enlarged orifice similar to that employed in [10] is examined and focus is given on elucidating the topological and dynamical features of the highly-fluctuating vortical structures, conventionally termed as string cavitation. For this reason, high-speed XPCI has been selected for the flow visualization, which allows the acquisition of high-speed, high-resolution radiographies with a relatively wide field of view.

Experimental Setup

The custom-made nozzle replica used in this investigation along with the upstream and downstream flow manifolds are shown in Fig. 1a, along with an indicative shadowgraphy image of the emerging two-phase flow. The prototype nozzle, the layout and main dimensions of which are shown in the detail-view of the figure, was manufactured from carbon fibre (TORAYCA TF00S), which, firstly, causes low radiation attenuation compared to metals and, furthermore, is able to withstand injection pressures up to 150 bar and outlet pressures up to 50 bar without deformation of its shape. A metallic needle with a hemispherical tip is inserted into the flow chamber (sac) upstream the injector hole and adjusted to a fixed position. A manifold layout precedes the examined nozzle configuration to ensure that the incoming flow is parallel and unperturbed, whereas the mechanism responsible for the adjustment of the needle is also seated on the flow device realizing the manifold, as can be seen on the top part of Fig. 1a.The hydraulic flow loop that was developed for the present investigation and is depicted on Fig. 1b, was operated at steady-state flow-rate conditions, while the fuel temperature was monitored through type-K thermocouples inserted in taps properly placed at the storage tank feeding the pump and the inlet manifold and adjusted to a specified set-point with the use of a heat exchanger and a PID controller. Control valves (flow regulators) placed at the outlet of the feed pump were employed for imposing the liquid volumetric flow rate, which was monitored through an axial-turbine flow meter. Liquid pressure at the inlet and outlet of the test bench was monitored through pressure transducers inserted in taps.
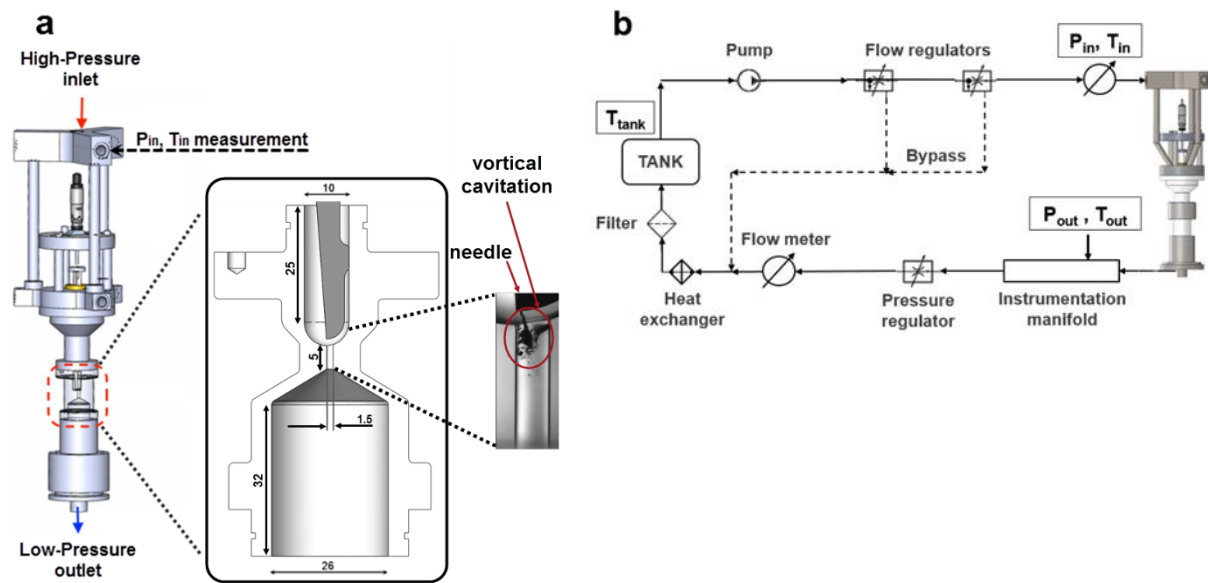

Figure 1. Schematic layout of (a) the test-bench and (b) the hydraulic flow loop.

The XPCI measurements were performed at the 7ID beamline, which has access to a white x-ray beam generated by an undulator in the APS electron storage ring. Referring to the beam pulsation mode, the so called "hybrid mode" allowing for time-resolved measurements, was selected. According to the specific operating mode, an x-ray pulse having a duration of 150 ps and carrying 16 mA of current is followed, after a gap of 1.569 µs, by eight short pulses, each one carrying 11 mA, separated by time intervals of 51 ns. The operating cycle is completed by an additional gap of 1.569 µs and hence its entire duration is equal to 3.682 µs. The attenuated x-ray beam, after its interaction with the injector orifice, impinges on the scintillator crystal, which converts the x-ray radiation to visible light (432 nm). The image is then reflected by a 45o mirror and captured by a CCD camera. In the specific investigation, only the bunch of eight pulses was utilized, which allowed a shutter exposure time of 347 ns to be achieved and hence the captured flow can be considered as frozen. Side-view radiographies at 67890 frames per second were obtained with a field of view of 2.56 mm x 2.56 mm discretized by 512 x 512 pixels, thus producing a spatial resolution of 5µm/pixel. However, it must be noted that the x-ray beam is collimated to a circular cross-section and therefore the

overall orifice length was segmented into five positions, which were radiated in a consecutive manner with overlapping regions between the locations.

The different test cases considered in the present evaluation are summarized in Table 1. As can be seen, four cases have been included in this study, corresponding to different values of the cavitation and Reynolds numbers. The position of the needle was adjusted to 0.5 mm upstream of its seat, since preliminary tests verified that strings with clearly discernible interfaces set in for the specific needle-lift value. The (nominal) Reynolds number characterizing the flow was defined on basis of the mean flow velocity $u_{mean} = {4\dot{V}}/{\pi D^2}$ and the nozzle diameter (*D=1.5 mm*) and lies in the range of 18000-35500; thus flow is expected to exhibit highly transient features within short time scales. Besides, the cavitation number was defined as follows:

$$CN = \frac{p_{inj} - p_{back}}{p_{back} - p_{sat}} \tag{1}$$

where p_{inj}, p_{back} and p_{sat} stand for the injection (upstream), back and saturation pressures, respectively. Based on the error propagation [11] due to the accuracy in the measurement of pressure, velocity and temperature, the uncertainty in the values of Re and CN are associated with global uncertainties of 3.5 and 5%, respectively. The working fluid employed for the investigation was commercial Diesel fuel provided by Lubrizol Corp., while the thermophysical properties required for the determination of Re and CN were calculated according to the data provided by [12]. The Diesel fuel density in the temperature range 312-315 K is of the order of 810 kg/m^3.

Table 1. Experimental test-cases investigated.

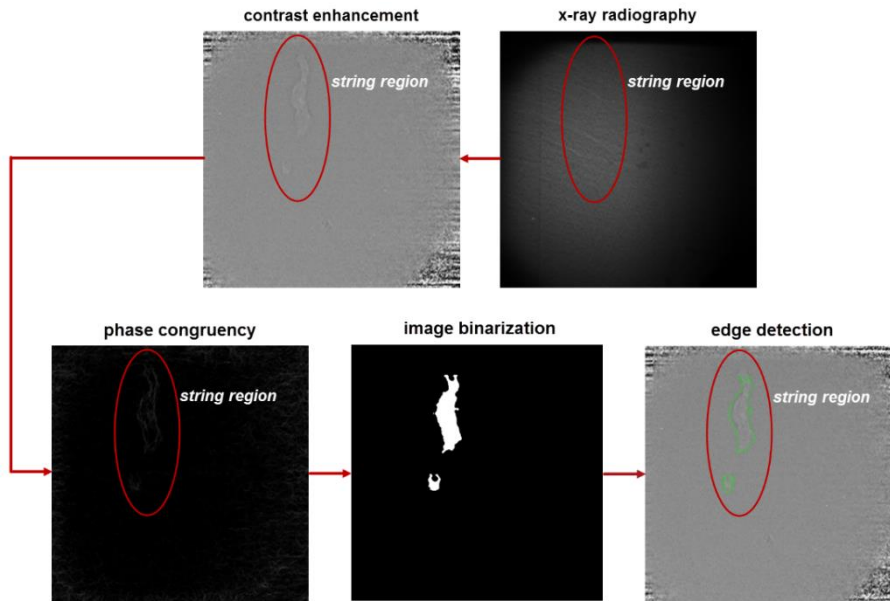| No.	lift [mm]	Re	CN	P_{inj} [bar]	P_{back} [bar]	T_{in} [ºC]
1		18000	1.6	14.56	5.64	40.7
2	0.5	35500	1.6	39.3	15.3	40.0
3		35500	2.0	36.4	12.2	42.3
4		35500	7.7	31.8	3.8	39.2

Figure 2. Sequence of the post-processing techniques employed.

Post-processing methodology

The camera used allows for the acquisition of 12-bit grayscale images, where a change in contrast signifies the presence of cavitation. A typical, "raw" x-ray radiography can be seen in the top-right part of Fig. 2, where the shadow of the needle is also visible at the top part of the figure. It can be easily perceived that the contrast fluctuation in the region of cavitation is low and therefore, in order to enhance contrast, the flow radiographies were divided by background images and the pixel brightness of each resulting image was adjusted to a specified range of values. All image-manipulation techniques were performed using the Image Processing toolbox in Matlab. A phase congruency method, as described in [13], was implemented to recognise the features of interest in the enhanced-

contrast images (bottom left part of Fig. 2). Subsequently, the image was binarized by applying a mean filter and proper thresholding [6], since after phase congruency the "string" edges appeared much brighter compared to the rest of the image. In subsequent step, the Canny's algorithm was employed to detect the edges of the identified structure. Finally, an additional ad-hoc algorithm was imposed to fill the gaps possibly arising in the detected edges and, thus, to produce a closed line corresponding to the string interphase (green line on right bottom part of Fig. 2).

Results

The actual string topology arising in the injector region adjacent to the needle tip (X=0) for Re=35500 is illustrated in Fig. 3. Fig 3a corresponds to a moderately cavitating flow (CN=1.6) and, as can be seen, a slender string sets in, which transforms to almost separated structures of irregular shape as the phenomenon progresses in time. It must be noted that post processing of the entire set of radiographies obtained for the specific location revealed a variability in the forms of the cavitating structures, comprising elongated strings, separated ligaments and clusters of bubbles. Increase of the cavitation number to 7.7 leads to the emergence of string that occupies a significant part of the injector hole cross-section having a relatively invariant core and, in general, a more stable topology compared to the respective for CN=1.6. The fact that the string attaches to the needle tip constitutes proof that the underlying cause is a longitudinal vortex, as according to the second Helmholtz theorem, a vortex filament must extend to a boundary or form a closed loop (see [14] for the flow field arising in a similar orifice layout). The strong centrifugal forces prevailing at the vortex core cause the liquid to cavitate. In the case of cloud cavitation, the cavity should be attached to the nozzle wall, as it arises due to the flow separation downstream the constriction. The temporally resolved images reveal significant interfacial fluctuations especially for the low value of the cavitation number due to the conflicting surface tension and viscous effects. It is a well-known fact that string cavitation exhibits a highly transient behaviour (e.g. refer to [10]). The string topology has been resolved in much more detail compared to conventional optical imaging and a far more complex topology has been revealed compared to typical shadowgraphy images (e.g. see Fig. 1). The interaction of the longitudinal vortices with the inherent flow turbulence causes the fluctuating appearance behaviour of the string cavities for low CN. In essence, vortices of smaller scale temporarily disrupt the coherence of the prevailing vortical motion thus causing the string to collapse.
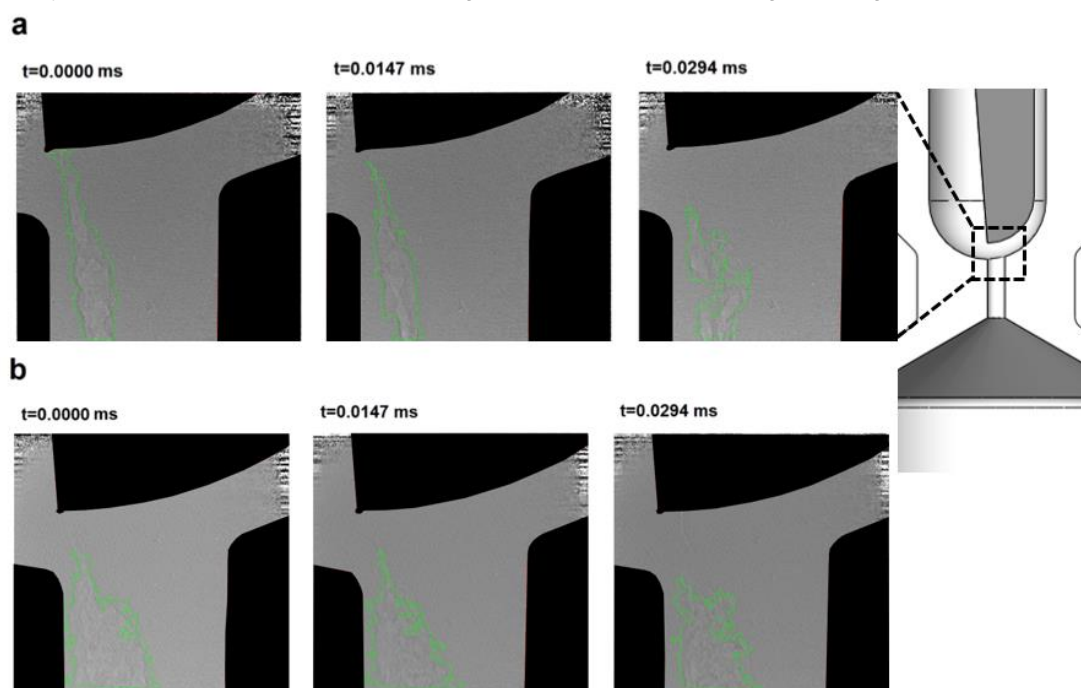

Figure 3. Topology of the cavitation cloud at the region adjacent to the needle tip for Re=35500: (a) CN=1.6 and (b) CN=7.7.

The spatial probability of vapour occurrence per pixel of the visualized region is depicted in Fig. 4a, as calculated by the averaging of 16000 radiographies for each region along the nozzle length also shown on the top part of Fig. 4a. Vapour occurrence probability is relatively low for CN=1.6 and reaches values up to 0.8 indicating that the formation of cavitating structures is a highly dynamical flow process. On the contrary for CN=7.7, the string core obtains a probability value of 1, signifying that a temporally-invariant, in the sense that its core does not exhibit significant fluctuations, string establishes with a well-defined interface to the surrounding liquid. It can be therefore

deduced that the string topology corresponds to a structure occupied by pure vapour. It is important to point out that the nozzle layout with the rounded inlet vertices (see nozzle wall at X=0) prevents geometrical cavitation to emerge. Hence, the onset of string cavitation is attributed solely to the secondary flow pattern, i.e., strong longitudinal vortices set in at the nozzle core due to the flow inherent instabilities and the effect of the geometrical constriction. The low pressure prevailing at the vortex cores causes the liquid to vaporize and the string to form. Furthermore, Fig. 4b depicts the image standard deviation, i.e. variability in pixel brightness compared to the mean image, which is indicative the magnitude of the shape variability that the vortical structures exhibit. Referring to CN=1.6, the highly fluctuating behaviour of the cavitating structures is clearly demonstrated, since the standard deviation obtains high values up to 0.5 in all the visualized positions. It can be deduced considering Figs. 3a and 4a-b regarding CN=1.6, that, despite the temporal variations in shape, a string-shaped structure is the prevailing cavitation form even for low cavitation numbers. For CN=7.7, the standard-deviation plot makes evident that the largest part of the string core remains invariant in time. Only the string part located close to the needle tip exhibits considerable temporal variation, while further downstream, high standard-deviation values occur at the outer edges.
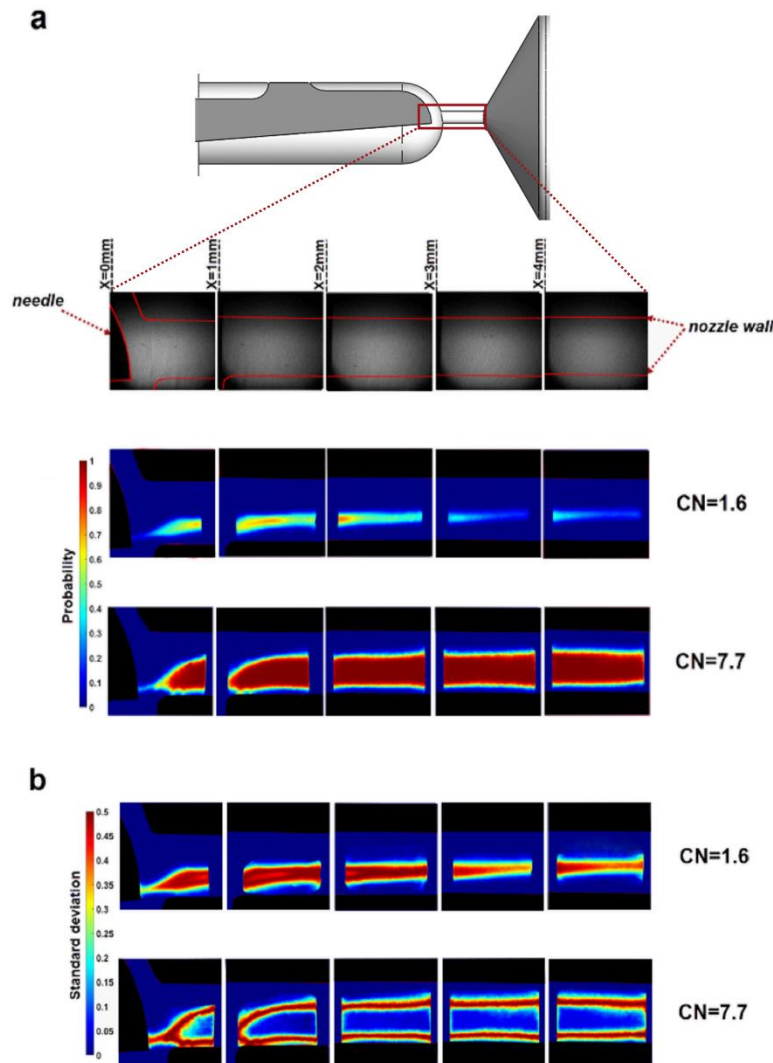

Figure 4. (a) Mean image and (b) standard deviation of the cavitating string for Re=35000.

As it has already been pointed out, string cavities for low cavitation numbers constitute dynamical flow features with highly varying morphology. In order to allow a straightforward comparison between the different cases investigated, the occurrence frequency of a repetitive, distinct flow process is presented in the dimensionless form of the Strouhal number ($St=fL/u$), with an associated uncertainty of the order of 3.5%. For instance, Fig. 5, illustrates the break-up behaviour of single strings into additional cavitating structures. The region immediately downstream the needle tip was selected due to the highly fluctuating string topology there, as verified by Fig. 4a. As depicted on Fig. 5a, string break-up is declared by examining frames (the control window is shown at the inset of Fig. 5b) corresponding to successive time instances and verifying that the detected edge has transformed from a single to two (or more)

closed loops. As made evident by Fig. 5b, depicting the break-up probability at a specific frequency, the string becomes more stable, i.e the break-up frequency decreases, as the Reynolds and cavitation numbers increase, while the repetitive pattern of the phenomenon is enhanced, as higher occurrence probabilities are obtained for the dominant frequencies. For instance, the cumulative probability the string break-up to occur at frequencies corresponding to St≤3 for Re=18000 and CN=1.6 is of the order of 0.6, whereas it reaches a value of 1 as Re and CN increase.

An additional quantity suitable for the characterization of the string dynamical behaviour is the lifetime period, i.e. the time interval between the string onset and collapse. Similar to the break-up frequency, the lifetime period was determined for each visualization location by assigning an appropriate control window and recording the average cavitation projected area within it. It is essential to clarify that for the low CN cases (CN≤2.0) examined, a plentiful of diverse structures emerge in the nozzle apart from coherent elongated, cavitating vortices. Hence, a conventional limit was set equal to 40% of the average projected string area (see Fig. 4), below which the string was considered to have lost its coherence. The limit specified was confirmed by observation of the actual radiographies, since once the area decreased below the limit, only ligaments or bubble clusters could be discerned in the control window.
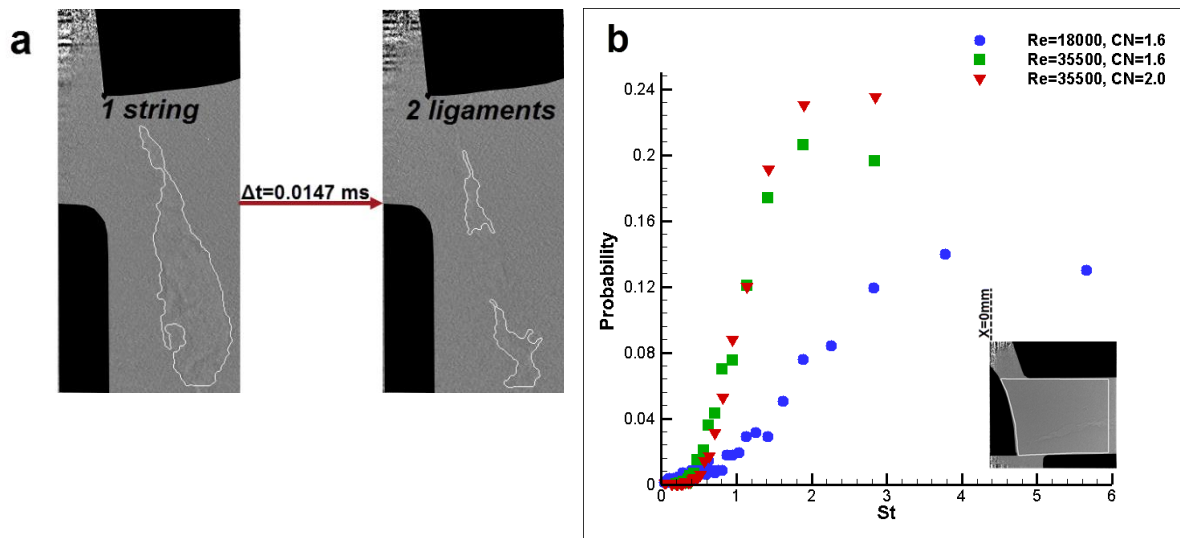

Figure 5. (a) Detection of string break-up and (b) effect of the flow conditions on the string break-up behaviour.

As shown by the data of Fig. 6a, increase of the Reynolds and cavitation number leads to increase of the string lifetime. For Re=18000 and CN=1.6 the maximum string life is, in essence, equal to 0.1 ms, while the cumulative probability of a string to exhibit a lifetime lower or equal to 0.03 ms is of the order of 0.73. It must be pointed that there is a 0.3 probability the string life to be even lower than the minimum lifetime that can be visualized by the method employed in this study. As the Reynolds number increases to 30000, while the CN is maintained constant, the distribution of possible lifetimes is shifted towards larger values approximately up to 0.3 ms, where the cumulative probability reaches a values approximately equal to 1. Yet once again about 30% of the strings recorded have a lifetime smaller than 0.03 ms. Increase of the CN value to 2.0 has a considerable effect on string stability, since the average lifetime is increased compared to CN=1.6, while the probability distribution becomes more even across the range 0.02-0.2 ms. The maximum probability is of the order of 0.09 for a lifetime approximately equal to 0.059 ms. The effect of the flow conditions on the string lifetime is justifiable since, increase of the Reynolds number, i.e. of the mean flow velocity, enhances the secondary-flow vorticity magnitude, which is responsible for the string formation. Furthermore, increase of the CN number, in other words, decrease of the back pressure leads to a pressure distribution in the injector-hole, which is closer to the cavitation threshold and thus a more insensitive cavity to flow perturbations establishes.

Besides, Fig. 6b indicates the string coherence does not decay simultaneously along the orifice length. It must be noted that the control windows were properly placed at each region of interest, so as not to include any overlapping areas of flow visualization. The string exhibits a similar behaviour in the first two regions downstream the needle tip (X=0.0 and 1.0 mm) with a relatively long lifetime, as the cumulative lifetime probability reaches a value of 1 for t=0.4 ms. On the contrary, at a further downstream location the string lifetime is much shorter, since its cumulative probability becomes equal to 1 at t=0.2 ms, and is indicative of a "flapping" behaviour at the string closure region. The inset of Fig. 6b depicting the string mean image at two different regions downstream the nozzle entrance verifies the string lifetime data. At the region between X=1.0 and 2.0 mm, the string existence probability is in general high

(>80%) almost at the entire length of the control window, whereas at a further downstream location (3.0mm≤X≤4.0mm) the lower half of the image, corresponding to the area where the flapping occurs, presents probability values in the range of 30-50%. Nevertheless, as also elucidated by Fig. 3, it must be emphasized that the actual cavitation topology in both regions is significantly different than the one inferred by the mean image.
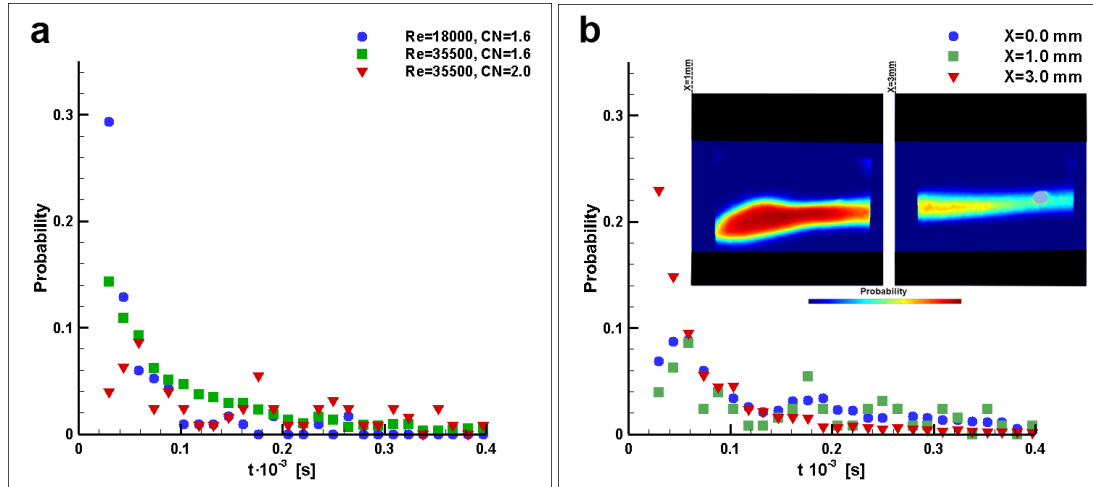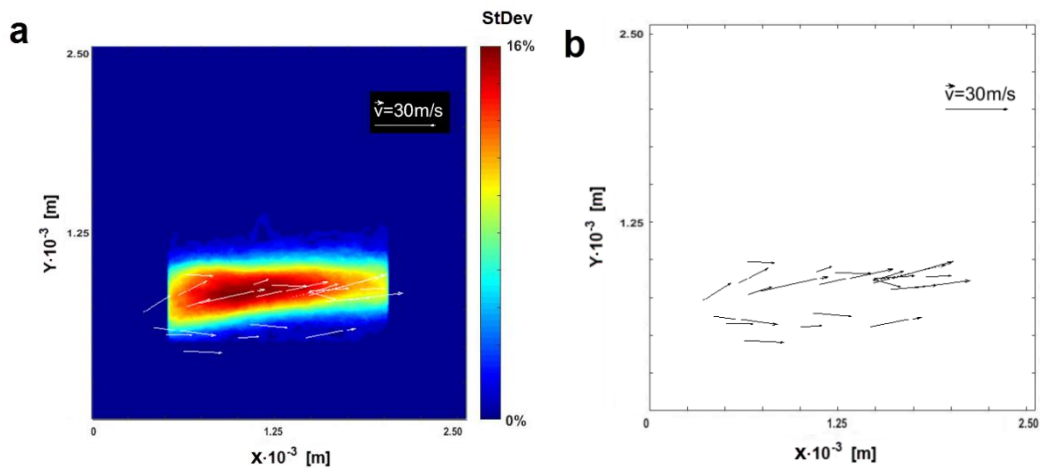

Figure 6. String lifetime: (a) effect of the flow conditions (X=1.0 mm) (b) probability for different positions along the channel length for Re=30000 and CN=2.0. For CN=2.0 a small artefact evident at the right part of the inset was detected and the respective area (shown in grey) was excluded from the control window.

XPCI employed in the present study enabled the resolution of scarce cavitating structures (small ligaments or bubble clusters) in reference to the low CN cases and of fine features of the string interface, in reference to high CN values. Such features served as points of reference, the trajectories of which allowed the derivation of the local, two-dimensional velocity field presented in Fig. 7 for two extreme cases in terms of Re and CN. The experimental uncertainty associated with the velocity values, stemming from the limitations posed by the spatial discretization and the exposure time, lies in the range of 3.5%-5.3% and 3.4%-4.0% for CN=1.6 (Fig 7a) and CN=7.7 (Fig. 7b), respectively. The maximum uncertainties are of course associated with the minimum velocity values for each case. Referring to both low and high-CN cases, regions where adequate points of reference could be identified have been selected to produce the respective velocity-vector plots, however a comparison between Figs 7a-b and 7c-d makes clear that the vector plot is much more thorough for CN=7.7. This is attributed to the fact that for Re=18000 and CN=1.6 only few scarce structures were identified, since for the specific flow conditions cavitating vortices are highly fluctuating and short-lived. On the contrary for Re=35500 and CN=7.7, a plentiful of distinct features could be identified at the string interface due to the high spatial resolution of XPCI and, therefore, a better representation of the local velocity field could be obtained. The average measured velocities for Re=18000 and 35500 are equal 28.8 and 60.2 m/s, while the respective nominal velocities based on the imposed flow rate and orifice cross section were calculated equal to 30.0 and 59.9 m/s. Hence, there is a strong indication that XPCI can be employed as a velocimetry method in cavitating flows, especially since conventional methods such as PIV, fail to produce measurements in regions of vapour.
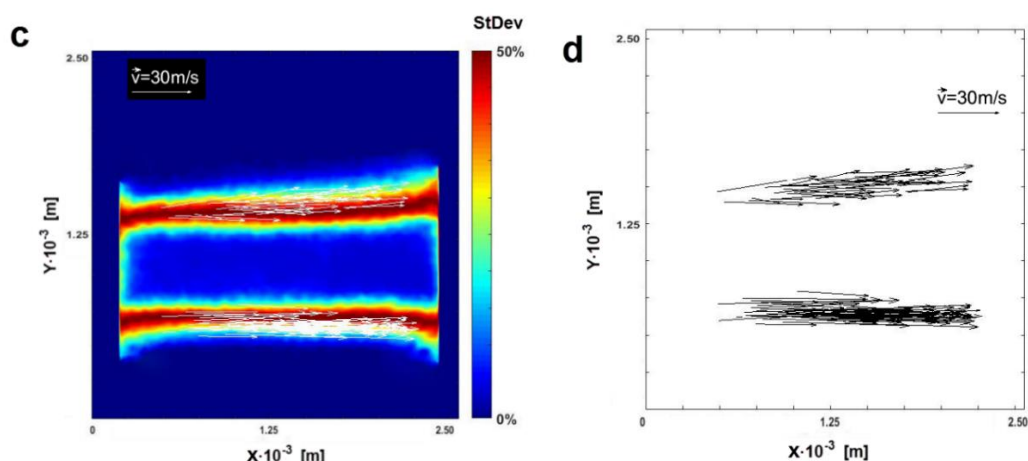
Figure 7. Local velocity field: (a-b) Re=18000, CN=1.6, X=1.0 and (c-d) Re=35500, CN=7.7, X=2.0.

Conclusions

The present study elucidated the spatial and temporal evolution of the cavitating strings emerging in an enlarged injector orifice with the use of XPCI. Post processing of the side-view radiographies obtained for the examined flow conditions and needle lift demonstrated that cavitation primarily emerges in the form of vortical structures of highly fluctuating and irregular shape for low Re and CN, while stable strings set in for high CN values with their interphase exhibiting high morphological variance. Average and standard deviation images of the string-shaped cavities were obtained for a wide range of conditions, while the spatial resolution of the present flow visualization technique enabled the capturing of fine features that cannot be resolved using optical imaging techniques, e.g. shadowgraphy or Schlieren. The temporally-resolved nature of the measurements allowed the characterization of the string dynamical behaviour and it was verified that the string breakup frequency decreases, while its lifetime increases, as the Re and CN increase. Finally, local velocity fields were measured in the string region for cases of low and high cavitation extent; the obtained average velocities compared well with the respective nominal values.

Nomenclature

CN	cavitation number	Re	Reynolds number
D	nozzle internal diameter [m]	St	Strouhal number
f	frequency [Hz]	u	axial velocity [m s^{-1}]
L	nozzle length [m]	v	kinematic viscosity [m^2 s$^-$

References

[1] Hult. J., Simmank, P., Matlok, S., Mayer, S., Falgout, Z., Linne, M., 2016, Experiment in Fluids 57, pp. 49.
[2] Arcoumanis, C., Gavaises, M., Flora, H., Roth, H., 2001, Mécanique & Industries 2, pp. 375–381.
[3] Mitroglou, N., Gavaises, M., Nouri J. M., Arcoumanis C., May 27. 2011, DIPSI Workshop.
[4] Petkovšek, M., Dular, M., 2013, Wear 300(1), pp. 55-64.
[5] Gavaises, M., Andriotis, A., Papoulias, D., Mitroglou, N., Theodorakakos, A., 2009, Physics of Fluids 21(5), pp. 052107.
[6] Mitroglou, N., McLorn, M., Gavaises, M., Soteriou, C., Winterbourne, M., 2014, Fuel 116, pp. 736–742.
[7] Moon S., 2016, Energy 115, pp. 615-625.
[8] Kastengren, A. L., Tilocco, F. Z., Duke, D., Powell, C. F., Zhang, X., Moon S., 2014, Atomization and Sprays, 24(3), pp. 251–272.
[9] Duke, D., Kastengren, A. L., Tilocco, F. Z., Swantek, A. B., Powell, C. F., 2013, Atomization and Sprays, 23(9), pp. 841–860.
[10] Mitroglou, N., Lorenzi, M., Santini, M., Gavaises, M., 2016, Experiments in Fluids, 57, pp. 175.
[11] Moffat, R.J., 1988, Experimental Thermal and Fluid Science 1, pp. 3-17.
[12] Kolev, N. I., 2007, "Multiphase Flow Dynamics 3: Turbulence, Gas Absorption and Release, Diesel Fuel Properties.", Springer, pp. 269-302.
[13] Kovesi P., 1995, Technical Report 95/4, The University of Western Australia.
[14] Koukouvinis, P., Mitroglou, N., Gavaises, M., 2017, Journal of Fluid Mechanics, 819, pp. 21-57.